Bulletin of Volcanology (2024) 86:27
https://doi.org/10.1007/s00445-024-01722-y

RESEARCH ARTICLE

Vulcanian eruptions at Sakurajima Volcano: geophysical data, numerical modelling, and petrological evidence

Takeshi Nishimura[1] · **Tomofumi Kozono**[1,2] · **Akiko Matsumoto**[3] · **Mitsuhiro Nakagawa**[3] · **Masato Iguchi**[4]

Received: 7 October 2023 / Accepted: 15 February 2024 / Published online: 4 March 2024
© The Author(s) 2024

Abstract

We investigated the magma conduit system beneath three active craters that have repeatedly generated Vulcanian eruptions at Sakurajima Volcano, Japan, by analysing seismic, infrasound, and tilt data. The hypocentres of the earthquakes associated with the Vulcanian eruptions are distributed separately at shallow depths of approximately 0.5 km beneath the craters. Infrasound indicated that the swelling of the crater floor starts approximately 0.2 s after the occurrence of earthquakes and that the eruption starts about 0.3 to 0.5 s later. During an eruption, tilt vectors at a station approximately 2.7 km far from the active craters indicated a deflationary trend directed toward one of the three active craters. A 1-D conduit flow simulation indicated pressure build-up at a depth of 0.4–1.0 km beneath the crater, consistent with previously reported pressure sources during eruptions detected by geodesy. Volcanic lapilli emitted from the three craters have the same chemical composition; hence, Vulcanian eruptions of all three studied craters originate from a common magma source.

Keywords Vulcanian eruption · Explosion earthquakes · Infrasound · Tilt · Whole rock analysis · Conduit flow model

Introduction

Analyses of volcanic earthquake, infrasound, and ground deformation data associated with volcanic eruptions provide direct information on the eruption dynamics (Dzurisin 2007; Watson et al. 2022; Zobin 2016). Vulcanian eruptions involve the rapid ejection of volcanic bombs, lapilli, and ash, thereby generating air shocks, and the fact that they often occur repeatedly has allowed for thorough investigations at various volcanoes (Clarke et al. 2015). Vulcanian eruptions are often accompanied by earthquakes called explosion earthquakes, infrasound that sometimes accompanies shock waves, and ground deformation caused by the inflation and deflation of the magma chamber and/or conduit (Nishimura and Iguchi 2011). Locating these sources in space and time is fundamental for clarifying the Vulcanian eruption mechanisms and understanding the magma conduit systems beneath the volcanoes.

The hypocentres of explosion earthquakes often occur at shallow depths just before and during eruptions, e.g. they have been recorded at approximately 1 km depth at the Ubinas Volcano, Peru (Inza et al. 2014), and Lokon-Empung Volcano, Indonesia (Yamada et al. 2016), and 0–2 km below sea level (b.s.l.) at Sakurajima, Japan (Ishihara 1990). Source mechanisms determined from moment tensor analyses often display volumetric changes that may indicate magma inflation/deflation, for example at Popocatépetl, Mexico (Chouet et al. 2005), Tungurahua, Ecuador (Kim et al. 2014), and Fuego, Guatemala (Lyon and Waite 2011). These results may allow interpretation of the configuration and size of a magma chamber and/or conduit. The single forces that represent counter forces of ejecta during eruption also explain the observed waveforms of explosion earthquakes, for example at Mt. St. Helens, USA (Kanamori et al. 1984; Kanamori and Given 1983), Asama and Tokachidake, Japan

Editorial responsibility: N. Pardo

✉ Takeshi Nishimura
takeshi.nishimura.d2@tohoku.ac.jp

[1] Department of Geophysics, Graduate School of Science, Tohoku University, 6-3 Aramaki-Aza Aoba, Aoba-Ku, Sendai 980-8578, Japan

[2] National Research Institute for Earth Science and Disaster Resilience, 3-1 Tennodai, Tsukuba, Ibaraki 305-0006, Japan

[3] Department of Natural History Sciences, Graduate School of Science, Hokkaido University, N10 W8, Kita-Ku, Sapporo 060-0810, Japan

[4] Sakurajima Volcano Research Center, Disaster Prevention Research Institute, Kyoto University, Kagoshima 891-1419, Japan

(Nishimura and Hamaguchi 1993), Asama, Japan (Ohminato et al. 2006), and elsewhere (Nishimura 1998).

Infrasound waveforms may inform the pressure release processes of volcanic eruptions (Kim et al. 2012), and are used for detecting the formation of shock waves (Morrissey and Chouet 1997). Infrasound analyses are also used for quantifying precise eruption onsets (Ishihara 1985; Yokoo et al. 2009), and it is known that the onset of infrasound is often preceded by seismic signals, for example at Sakurajima, Japan (Ishihara 1985), and Stromboli, Italy (Ripepe et al. 2001). These studies suggest that the eruptions are triggered by subsurface processes and not by rupture of the crater floor. At Colima Volcano, Mexico, long-period seismic waves are often observed before the onset of eruptions, implying fluid motion in the conduit (Zobin et al. 2008). Studies have shown that long-period seismic signals prior to eruptions may be related to magma and/or exsolved fluid behaviour in the conduit/magma chamber, such as slug flow, churn flow, and fragmented magma flow, e.g. at Stromboli (Ripepe et al. 2001; Sugimura et al. 2021), Aso (Ishii and Yokoo 2021), and Colima (Zobin et al. 2008) volcanoes. At Sakurajima Volcano, studies have revealed pressure waves or fluids propagating at a speed of approximately 1 km/s in the conduit before eruptions (Ishihara 1985; Tameguri et al. 2002); however, such high-speed pressure waves may not propagate in the vesiculated magma in the conduit just before the explosion due to its poor elastic properties (Marchetti et al. 2004).

Ground deformation indicating inflation and deflation associated with eruptions is related to pressurisation caused by magma supply and withdrawal, respectively. Inflation preceding volcanic eruptions is useful for eruption forecasting (Kamo and Ishihara 1986; Nishimura et al. 2012, 2013). For example, Sakurajima Volcano inflates for a few tens of minutes to hours before a Vulcanian eruption because of the accumulation of magma, and deflates during the eruption due to the removal of magma from the conduit and magma chamber (Kamo and Ishihara 1986; Iguchi et al. 2013). Deflation is also useful for evaluating the volumes of ejecta and their relationship to the erupted volumes (Kozono et al. 2014; Hreinsdóttir et al. 2014).

Sakurajima Volcano is amongst the most active volcanoes in Japan. According to Kobayashi et al. (2013), the geological feature and eruptive activity of the volcano are summarised as follows. The volcano is a post-caldera volcano of Aira Caldera (29 ka) located at the southern edge of the caldera. The volcano is composed of two adjacent stratovolcanoes: Kitadake (the northern peak, which is 1117 m above sea level) and Minamidake (the southern peak, which is 1040 m above sea level) with many parasitic cones on the flank. All the eruptive products of the volcano are andesite to dacite in composition. The eruptive activity of the Kitadake Volcano started at 26 ka with repeated Plinian eruptions with lava effusion. The activity of the Minamidake Volcano began at 4.5 ka and has continued until the present. Four large eruptions occurred in CE 764, 1471, 1779, and 1914. In each event, a Plinian eruption ejected voluminous pumice, followed by effusion of lava flows. In CE 1946, an eruption occurred on the eastern flank (from Showa crater), resulting in effusion of lava flows. The recent eruptive activity of Sakurajima Volcano is mainly characterised by Vulcanian eruptions, which first began at the summit crater, Minamidake crater, in CE 1955. The activity has continued at the Minamidake and Showa craters with temporary pauses. Annual numbers of the Vulcanian eruptions now reach a few hundred times or more according to the Bulletins on Volcanic Activity of the Japan Meteorological Agency (JMA) that are monthly reported on the JMA website (https://www.data.jma.go.jp/vois/data/tokyo/STOCK/monthly_v-act_doc/monthly_vact.php).

The volcano is well monitored and studied, using not only geophysical observations, i.e. seismic, acoustic, and geodetic measurements, but also geochemical and geological analyses (Iguchi et al. 2013). Vulcanian explosions at Sakurajima Volcano are often preceded by inflation, which lasts between 10 min and several hours (Kamo and Ishihara 1986; Ishihara 1990). Explosion earthquakes occur approximately 1 s before the eruptions (Ishihara 1990; Tameguri et al. 2002), and then, volcanic rocks are rapidly ejected from the vent, while occasionally generating significant shock waves (Ishihara 1985). Consequently, the deflation occurs for a few tens of minutes, causing subsidence of the ground surface (Kamo and Ishihara 1986). Recently, the amount of volcanic ash effused during eruptions has been quantified by analysing seismic and geodetic measurements (Iguchi 2016). In addition, a monitoring system for volcanic ash using Doppler radars and disdrometers has been deployed at the volcano, and the spatio-temporal distribution of volcanic ash may be forecast (Iguchi et al. 2019; Maki et al. 2019).

In recent years, the activity of Sakurajima Volcano has resulted in changes to the volcano's active craters. Here, we determine the hypocentres of explosion earthquakes beneath multiple craters during Vulcanian eruptions occurring from 2012 to 2020. It is well known that volcanic structures are heterogeneous and that the vertical velocity change is important for determining the depths of hypocentres; hence, we accurately determined the hypocentres using a velocity structure that was recently obtained from artificial source experiments. We further analysed the infrasound and ground deformation associated with Vulcanian eruptions and discussed the eruption mechanism and magma reservoir/conduit system at Sakurajima Volcano using a multi-phase conduit flow model, as well as whole rock compositions of volcanic lapilli emitted from three different craters.

Methods

Hypocentre determination of explosion earthquakes

Volcanic explosions are routinely reported by the Kagoshima Meteorological Office of JMA, which is located about 11 km west southwest of the volcano. More than 6000 explosions or eruptions were reported between 2012 and 2020. Showa crater was active until 2017, whereas Minamidake A and B craters were active since 2018 (Fig. 1a). We downloaded the seismic waveforms of six JMA stations deployed on the flank of Sakurajima Volcano, which are located at distances of about 2.8–4.8 km from the Minamidake (Fig. 1b), and selected explosion earthquakes with good signal-to-noise ratios. The amplitudes of the P-waves of explosion earthquakes are very small, especially at distant stations; however, we could measure the onset times of the P-waves by visually selecting at least five stations for 150 explosion earthquakes (Fig. 1c).

Seismic velocity in previous studies (Ishihara 1990; Iguchi 1994) used a homogeneous structure with a P-wave velocity of 2.5 km/s, whereas this study used a velocity structure derived from the analyses of an active experiment using artificial sources conducted at Sakurajima Volcano in 2008 (Miyamachi et al. 2013). More than 300 seismometers were deployed along lines in and around Sakurajima Volcano and Aira Caldera, and dynamites embedded at depths of a few tens of meters were used to generate seismic waves. The P-wave onsets were manually read by the researchers

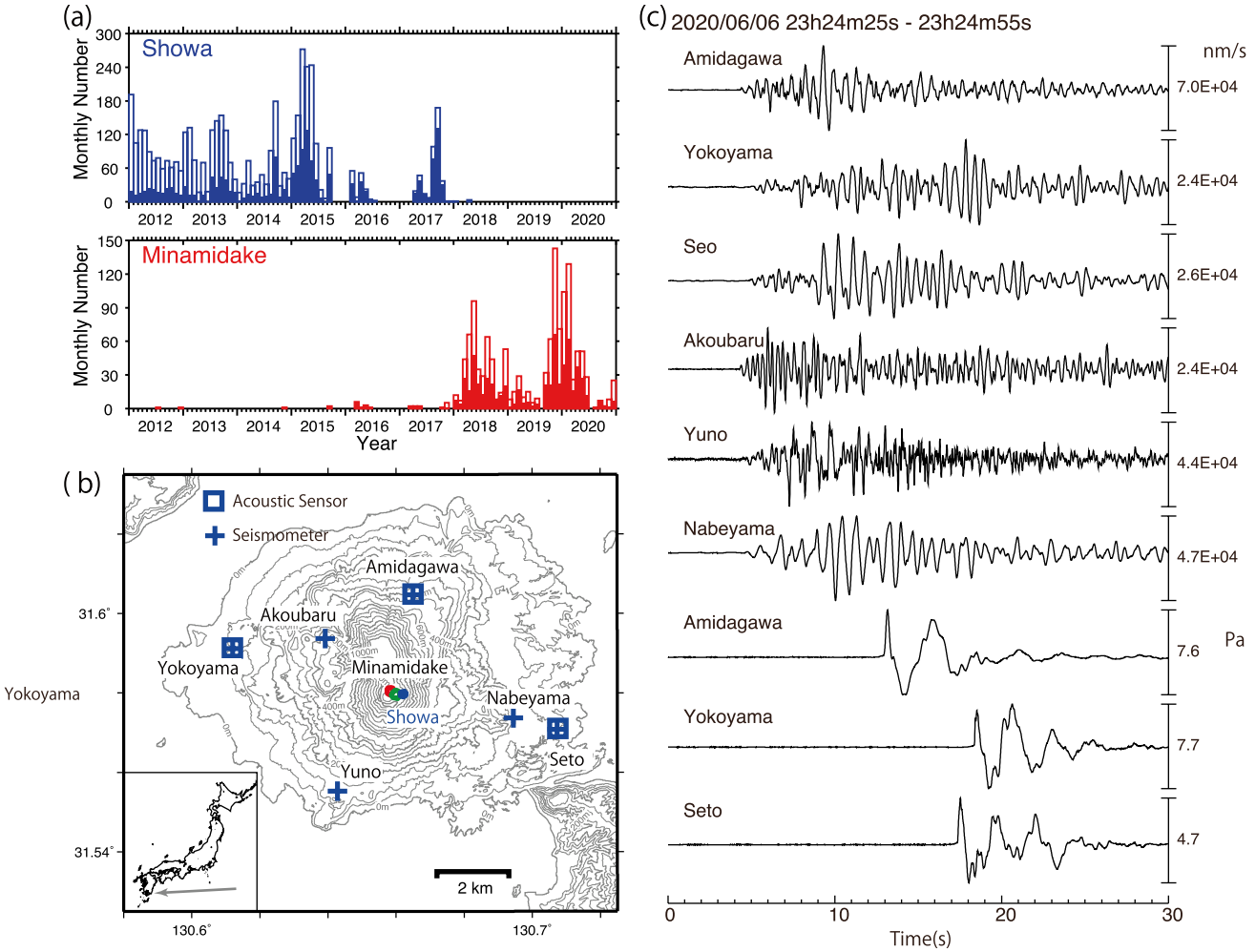

Fig. 1 **a** Eruptive activity of Sakurajima Volcano. Solid and open bars represent the numbers of eruptions and explosions, respectively. 'Explosion' is the eruption with large seismic and acoustic signals, and 'eruption' is the other, which are classified by the Kagoshima Meteorological Office. **b** Locations of the monitoring stations. Cross and square symbols represent the seismic and infrasound stations, respectively. Red, green, and blue circles indicate the locations of Minamidake A and B, and Showa craters, respectively. **c** Example of seismic and infrasound waveform generated by a Vulcanian eruption

participating in the experiment and the refraction method revealed the P-wave velocity structure beneath the survey lines. At Sakurajima Volcano, three survey lines were set and a unified P-wave velocity model was presented. The structure shows low P-wave velocity of 1.5–1.8 km/s in the shallowest layer with a thickness of approximately 100 m. Then, the P-wave velocity increases from 2.0 km/s at the ground surface to 2.8 km/s in the first layer at 1 km b.s.l., 3.6–4.6 km/s in the second layer between approximately 1 and 2 km b.s.l. and 4.6–5.0 km/s in the third layer at approximately 3 km b.s.l. In this study, we neglected the surface low-velocity layer, because the seismometers of the JMA stations were set at a depth of approximately 100 m, and set the P-wave velocity at the ground surface to 2 km/s. The velocity increased linearly with depth in each layer (Fig. S1).

We calculated the travel times of P-waves to include the seismic velocity beneath the volcano using the TOMO3D software (de Kool et al. 2006). Because the software uses a finite difference method, we were able to directly include the volcano topography and calculate the travel times from a hypocentre above sea level to seismic stations. An example of ray paths from seismometers beneath an active crater is shown in Fig. S1. Because of the velocity gradient, the seismic rays first moved downward from the hypocentres and reached the stations. We set grid points every 0.01° in the east–west and north–west directions, and 0.1 km in the vertical direction to calculate the travel times from each grid point to each station. We searched for grid points showing the minimum residuals between the observed travel time differences between the six stations and the calculated values. Subsequently, we applied the least-squares method to obtain the best solution for the location and onset time by using the velocity gradients for the horizontal and vertical directions, which were calculated from the travel times at nearby grid points.

Analysis of infrasound data

We estimate the lead time from the origin times of the hypocentres of explosion earthquakes to the eruption occurrence time using the arrival times of infrasound observed at three JMA stations to understand the conduit process just before eruption. The acoustic sensors deployed on the flank of the volcano detected clear infrasound signals, in which the waveforms were characterised by a gradual pressure increase with a small amplitude, followed by a rapid pressure increase with a large main wave (Fig. 2a). The former, which is the preceding phase, is considered to be provoked by the deformation of the crater floor (Yokoo et al. 2009), whereas the latter is caused by a rapid pressure release followed by a rupture of the crater floor, which may sometimes generate a shock wave (Ishihara 1985). The time difference between the former and latter waves ranged between 0.1 and 0.5 s, while the former wave was sometimes not detectable.

We first determined the onset (t_e) of the preceding phase of the infrasound. Because of the small amplitude of less than a few Pa at a distance (2.7 km) from Amidagawa station, the preceding phase can be infinitesimal waves that propagate at a speed independent of the amplitude of the wave. Since the infrasound wave speed (v_a) depends on temperature ($v_a[\mathrm{m/s}] = 331.15 + 0.61T[^\circ\mathrm{C}]$), we substituted the atmospheric temperature at a height between the active crater and station for the temperature along the path, using the temperature recorded at Kagoshima by JMA and the altitudes of the crater and stations. To consider the effect of wind speed, we simultaneously estimated the infrasound onset time, the average speed, and the direction of the wind that blows around Sakurajima Volcano by applying a grid search to the observed infrasound onset times. The estimated wind speeds and directions are presented in Fig. S2.

Analysis of tilt records

We examine whether each crater is connected to its own magma chamber extending down to a few kilometre depth by analysing the tilt vectors at Amidagawa station, which is located in the northern flank at a distance of 2.7 km from these craters. The tilt vector directions at Amidagawa station would be different if the three active craters were almost aligned in the east–west direction and had their own chambers connecting through their own conduits. The other two tilt meters operating at the Seto and Yokoyama stations were too far apart to record explosion signals.

Tilt signals associated with eruptions at Amidagawa station exhibited amplitudes of 10^{-8} to 10^{-7} rad. However, the signals were contaminated with not only tidal signals from M_2 and O_1 tides, but also by long-period (i.e. a few hours) noise, likely originating from the sea water load flowing around the volcanic island, forming a narrow water channel in Kagoshima Bay. Hence, after removing the M_2 and O_1 tidal signals, we visually checked the tilt records and selected data with relatively good signal-to-noise ratios before and after the explosions (Figures S3 and S4).

Whole rock analysis of the lapilli samples

We examine whether the volcanic lapilli emitted from the three craters originate from a same chamber or from their own chambers. Lapilli samples emitted from Minamidake and Showa craters between 2012 and 2020 were collected from around the volcano at approximately the same time as that of each eruption. The samples were crushed in an iron mortar and washed with ultrasonic water. After drying at 100 °C in an oven, the samples were crushed by an agate mill making powders. The whole rock compositions

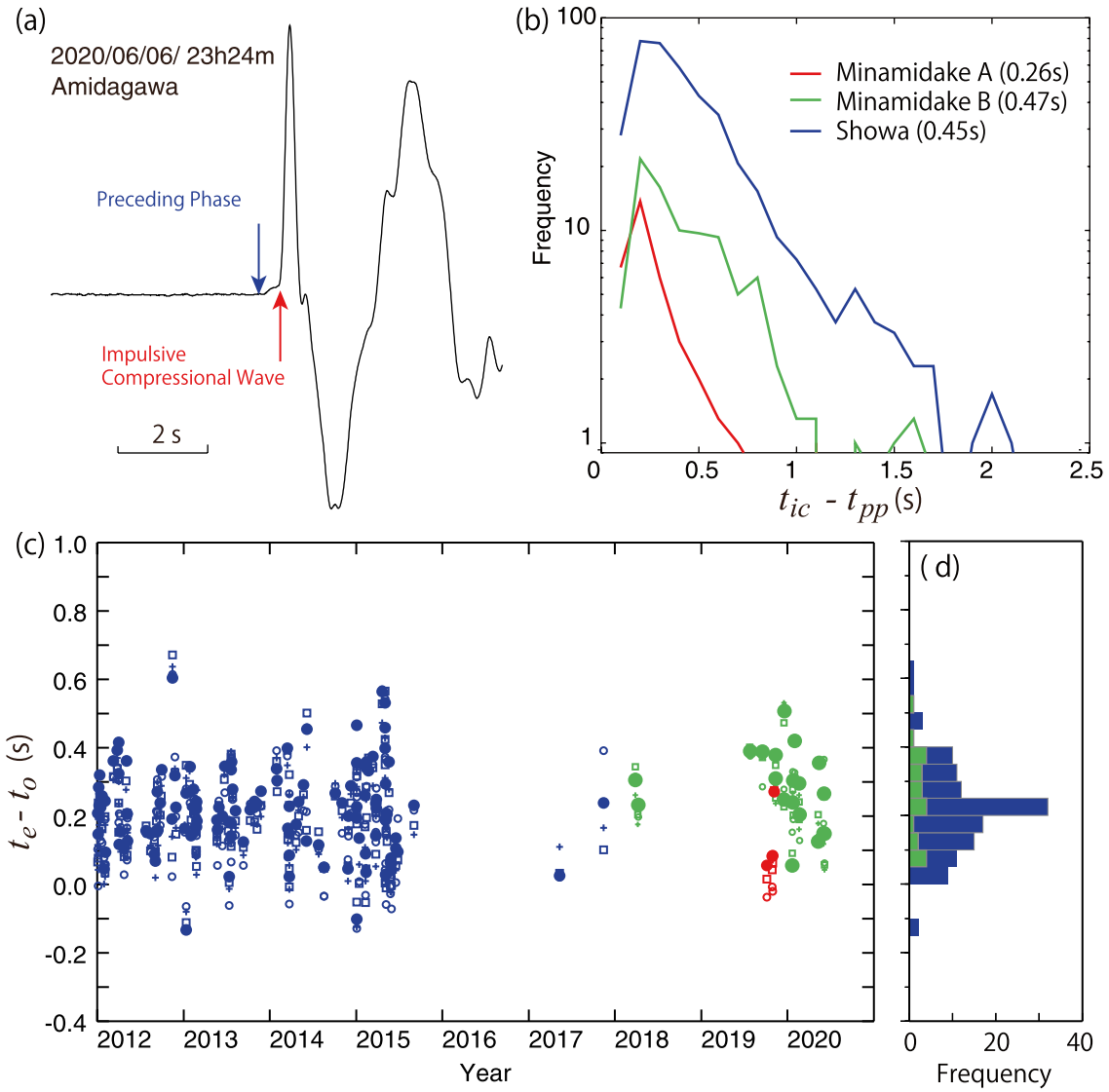

Fig. 2 **a** Preceding phase and impulsive compressional wave. **b** Histogram of the time differences ($t_{ic} - t_{pp}$) between preceding phase and impulsive compression wave of infrasound generated by explosions from the three craters. The numbers in brackets are the characteristic times required for destruction of the crater floor. **c** Temporal changes of lead times from the origin time of explosion earthquake (t_o) to the onset (t_e) of the preceding phase of the infrasound (t_{pp}). Red, green, and blue solid dots represent the data of Minamidake A and B, and Showa craters, respectively. These data are corrected by temperature and wind (see text for details). Open circles and squares, and plus symbols are the lead times estimated from the data at each station (Amidagawa, Yokoyama, and Seto stations) with a temperature correction. **d** Histogram of the lead times with a temperature and wind correction. Data of Minamidake A crater are not shown because of their small amount

of the lapilli samples were determined by X-ray fluorescence using a Spectris MagiX PRO system with an Rh tube at Hokkaido University. Major elements were measured using glass beads diluted to a 1:2 ratio and prepared by fusing the samples with an alkali flux (a 4:1 mixture of lithium tetraborate and lithium metaborate). All data are listed in Table S1.

Numerical simulation of one-dimensional steady conduit flow model

We investigate the features of the pressure source in the conduit prior to Vulcanian eruptions using a one-dimensional steady conduit flow model (Kozono and Koyaguchi 2012; Anderson and Segall 2011). By referring to the

observed solid plug formation at the crater floor (Yokoo et al. 2009), we considered a model composed of viscous flow and solid plug regions at deeper and shallower levels of the conduit, respectively. Detailed formulations of the model are shown in Appendix 1.

For the viscous flow region, we model a one-dimensional steady flow through a cylindrical conduit based on Kozono and Koyaguchi (2012). Prior to Vulcanian eruptions, magma has a low ascent velocity, with timescales for volatile exsolution and crystallisation much longer than the timescale for magma ascent. Efficient gas escape is considered to occur in the conduit. We assume equilibrium vesiculation and crystallisation, and consider a vertical gas escape by allowing relative motion between the gas and the melt-crystal mixture. We also consider the dependences of melt viscosity on dissolved H_2O and temperature (Giordano et al. 2008), and the dependences of magma viscosity on crystallinity, aspect ratio of the crystal, and strain rate (defined as the ascent velocity divided by the conduit radius) (Frontoni et al. 2022). Crystallinity was expressed as a function of pressure, which was obtained from exponential fitting for the simulation of isothermal decompression-driven crystallisation using the rhyolite-MELTS software (Fig. S5a) (Gualda et al. 2012). From the simulation result, we also obtained a power-law fitting function for the dissolved H_2O concentration as a function of pressure (Fig. S5b) and a third-order polynomial fitting function for the melt viscosity as a function of dissolved H_2O, following Giordano et al. (2008) (Fig. S5c). For the solid plug region, the motion of the solid plug is based on the model by Anderson and Segall (2011), in which the solid plug is subjected to an upward force due to magma pressure in the conduit, and downward force due to the weight of the plug and frictional resistance due to slip on the marginal faults. We assume that the transition from a viscous flow to a solid plug occurs when the viscous resistance in the viscous flow matches the frictional resistance of the solid plug (Schneider et al. 2012).

The conduit length was set to 4000 m based on geodetic observations revealing a deep pressure source (Hotta and Iguchi 2021). The magmatic parameters were set according to petrological observations of the ash samples emitted from Minamidake and Showa craters (Miwa et al. 2013; Matsumoto et al. 2016): the temperature was set to 1000 °C based on the two-pyroxene geothermometer (Putirka 2008), and the melt compositions, which were used as initial conditions in the crystallisation simulation, were set based on the average groundmass (glass + microlite) composition (Miwa et al. 2013; Matsumoto et al. 2016). The crystallinity in the magma chamber (i.e. the phenocryst volume fraction) was set to 30 vol% based on the phenocryst mode analysis. The initial bulk H_2O content was set to 4 wt% to achieve water-saturated magma in the magma chamber.

Results

Hypocentres of explosion earthquakes associated with eruptions at three active craters

The obtained hypocentres are shown in Fig. 3, and the errors (one standard deviation) of the hypocentre locations are shown as histograms (Fig. S6). The Kagoshima Meteorological Office defines two distinct craters (Minamidake and Showa craters) for the eruptions in 2012–2019 and three craters (Minamidake A and B, and Showa) for the eruptions in 2020. Comparing them with the arrival time differences of infrasound recorded at the three JMA stations (Fig. 1b), we determined the erupted crater for each explosion earthquake during the observation period. Figure 3 plots the hypocentres with different colours by the crater erupted. Evidently, the hypocentres of the explosions occurring at Minamidake A and B, and Showa craters are located closely to the corresponding craters aligned from west to east. The hypocentres are located separately, beyond the estimation errors of a few hundred meters (Fig. S6). The depths of the hypocentres are very shallow: 0.2–0.8 km beneath the craters (i.e. 0.0 to 0.6 km above sea level).

The depths of hypocentres depend on volcanic structures, especially at shallow depths around the active craters, which may not be well determined by the refraction survey because seismometers were not deployed around the crater due to the high explosive activity of Sakurajima Volcano (Miyamachi et al. 2013). Setting the lower/higher velocity of the ground surface may result in shallower/deeper hypocentre estimate.

Results of infrasound data analysis: rupture of the crater floor and eruption

Figure 2c and d show a plot of the lead time ($t_e - t_o$) determined from the onset of the explosion earthquake (t_o) to the onset of the preceding phase of the infrasound (t_{pp}). The lead time ranged from 0.0 to 0.4 s, with an average of 0.2 s. No significant difference was observed between the explosions at the three craters. The lead time may correspond to the lapse time at which the pressure wave/flow reaches the crater floor from the hypocentre. Since the maximum speed of the pressure wave can be 1–2 km/s, which is the P-wave velocity of magma or surrounding rocks, the depths of hypocentres are equivalent to depths between 0.2 and 0.4 km beneath the crater floor. These estimates are consistent with the results of the previous section (hypocentres determined from the P-wave arrival times). When the seismic source region consists of gas

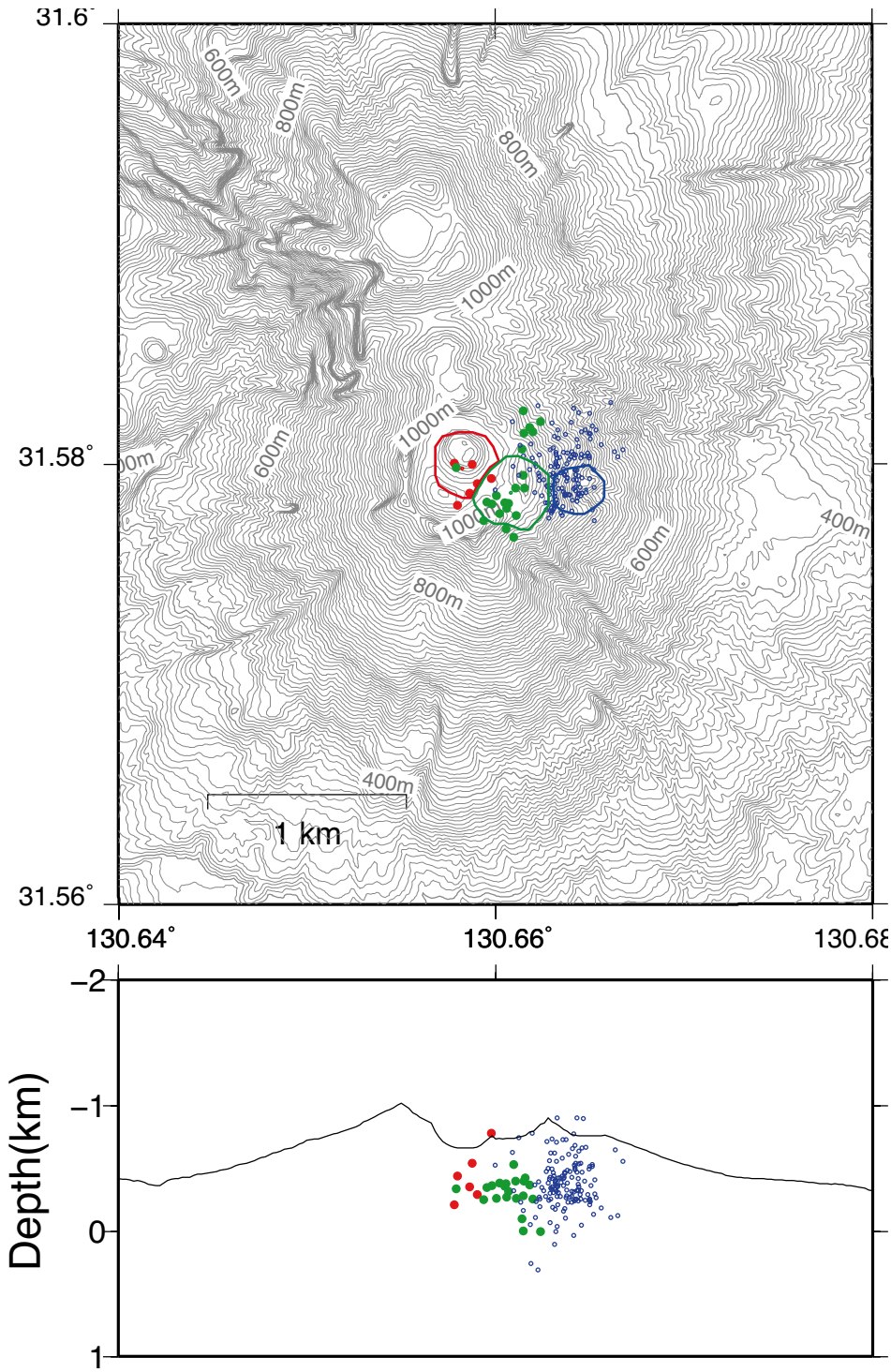

Fig. 3 Hypocentres of volcanic explosion earthquakes. Red, green, and blue circles represent the hypocentres of explosion earthquakes associated with Vulcanian eruptions occurring at Minamidake A and B, and Showa craters, respectively. Red, green, and blue lines in the top panels indicate the craters of the hypocentres. Several hypocentres located above the ground surface are due to hypocentre determination errors

and/or vesiculated magma, the speed of the pressure wave is smaller (i.e. of the order of 100 m/s; Kieffer 1984; Ichihara and Kameda 2004), and the source depths of hypocentres are much shallower, i.e. approximately a few tens of meters.

Next, we examined the time difference between the onset of the preceding phase (t_{pp}) and the onset of the impulsive compressional wave (t_{ic}) to quantify the time required to rupture the crater floor after the triggering of the explosion earthquake. We analysed not only the data in Fig. 3, but also other data with good signal-to-noise ratios because the time differences were measured only from the infrasound data. For the data for which we could measure both t_{pp} and t_{ic}, the time differences mostly ranged between 0.0 and

0.5 s (Fig. 2b). The histograms of the time differences of all eruptions at Minamidake A and B, and Showa craters obey exponential distributions ($N = N_0\exp(-t/\tau)$) (Fig. 2b). The characteristic times required for destruction of the crater floor (τ) were estimated from the data at the three stations as 0.26, 0.47, and 0.45 s for the Minamidake A and B, and Showa eruptions, respectively. The characteristic times of Minamidake B and Showa craters were almost the same, suggesting that the rupture processes and physical properties of their crater floors are similar. The characteristic time of Minamidake A crater was shorter than those of the others; however, this may be due to the scarcity of data. The characteristic time may not directly represent the time necessary for destruction, as Ishihara (1985) observed shock waves radiating from active craters and measured a propagation velocity of 441 m/s in the atmosphere, approximately 800 m above the crater, using video images. In this study, we estimated the difference in propagation time using the shock wave model of Médici et al (2014). The amplitude of infrasound generated by the eruptions from 2012 to 2020 is approximately one order of magnitude smaller than that in the 1980s, and the pressure amplitude at Amidagawa station ranges from approximately 1 to 100 Pa. The distance (D_t) of the transition from supersonic to sonic flow was estimated to be 8 m for 10 Pa, and 77 m for 100 Pa. Assuming a propagation velocity of 400 m/s for the supersonic wave, we estimated the difference of propagation time to be 0.006 s for 10 Pa, and 0.060 s for 100 Pa. This suggests that shock waves may have been generated from the active craters; however, their effect on the propagation velocity (i.e. the time required for destruction of the crater floor) was small.

Results of tilt record analysis: magma reservoir/conduit depressurisation during eruption

Figure 4 shows the tilt vectors before and after several Vulcanian eruptions at Minamidake A and B, and Showa craters. The observed tilt vectors are directed approximately along the NS to NNE–SSW directions, with uplift toward the active craters before eruptions, showing zigzag traces because of long-period noise. The tilt vectors then change in the opposite directions, with a downward trend toward the active craters. These deflation phases exhibit relatively short durations of a few tens of minutes; hence, the tilt vectors are not disturbed by noise, while being directed toward Minamidake A crater for all explosions occurring at Minamidake A and B, and Showa craters. Furthermore, the tilt vectors soon begin to exhibit a downward trend toward Minamidake A crater, without significant directional changes during the deflation phase, suggesting that the source soon starts to

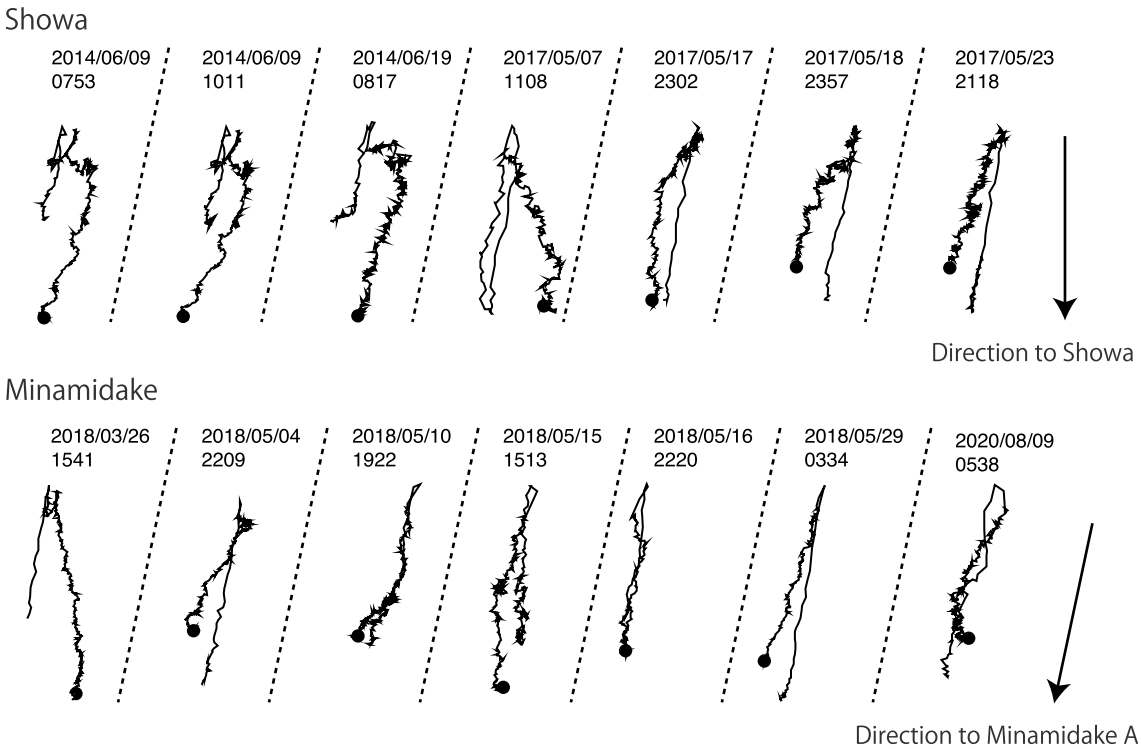

Fig. 4 Examples of tilt vectors at Amidagawa station before and during eruption. The solid dots represent the beginning of the data. The directions toward Showa crater and Minamidake A crater are indicated by an arrow at the right side in the upper panel and lower one, respectively. Dotted lines are additional ones to compare the direction toward Minamidake A crater with each of tilt vectors

deflate after the occurrence of an eruption. These characteristics strongly suggest that the three active craters have the same conduit feeding system; however, their associated vertical extent cannot be inferred from tilt data analyses at one station.

Compositions of volcanic lapilli emitted from Minamidake and Showa craters

Matsumoto et al. (2013) indicated that the whole rock compositions of juvenile materials from Minamidake craters between 1955 and 2000 were consistent with the juvenile material emitted from Showa crater between 2007 and 2011. We examine juvenile material emitted from the Showa and Minamidake craters between 2012 and 2020. Figure 5 shows a Harker diagram of whole rock compositions of juvenile materials since 1957. Results showed that all juvenile material from Minamidake and Showa craters has a very similar chemical composition. This result strongly suggests the magmas originate from the same conduit system.

Results of numerical simulation of one-dimensional steady conduit flow model: pressure build-up in the conduit

Using the conduit flow model, we obtained the relationship between the pressure in the magma chamber and the magma flux (Fig. 6a), in which the conduit flow satisfies the condition that the conduit length is equal to the sum of the lengths of the viscous flow and solid plug regions. This relationship was used to select a stable steady solution: the conduit flow is stable when there is a positive correlation between the

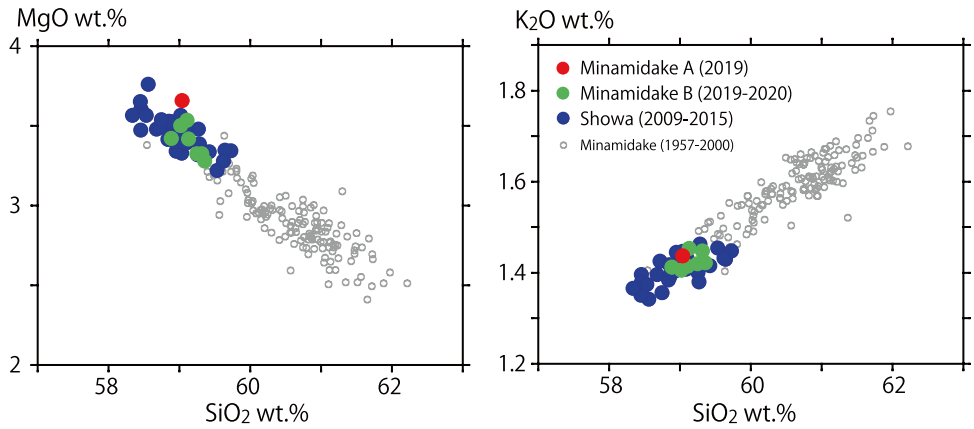

Fig. 5 Harker diagrams of whole rock compositions of juvenile materials since 1957. Red, green, and blue solid dots are the data of Minamidake A and B, and Showa craters, respectively. Open black circles are data from Minamidake A and B craters taken from Matsumoto et al. (2013)

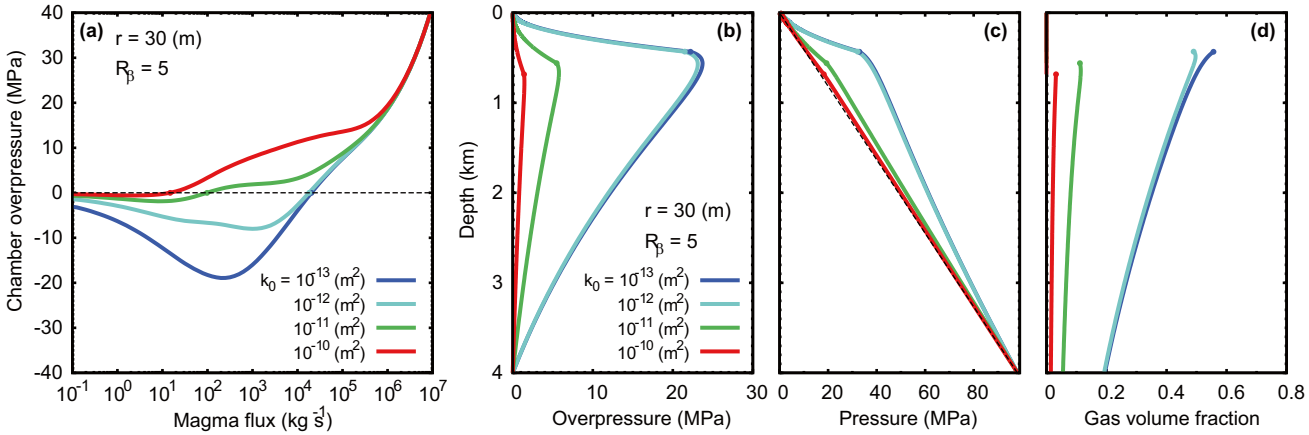

Fig. 6 Numerical results of the one-dimensional steady conduit flow model for $r=30$ m and $R_\beta=5$ with varying k_0. Here, r is the conduit radius, R_β is the aspect ratio of crystals that controls the effect of crystals on magma viscosity (Frontoni et al. 2022), and k_0 is the permeability coefficient controlling the scale of the permeability (Costa 2006). **a** The relationship between the chamber overpressure with respect to the lithostatic pressure and magma flux, where solid circles correspond to selected stable steady solutions with lithostatic chamber pressure. **b**–**d** Overpressure with respect to the lithostatic pressure (**b**), pressure (**c**), and gas volume fraction (**d**) with depth for the stable solutions selected in **a**. The solid circles in **b**, **c**, and **d** represent the transition points from the viscous flow to the solid plug, and the dashed line in **c** is the lithostatic pressure

chamber pressure and the magma flux (Kozono and Koyaguchi 2012). In this study, we selected a stable solution with a lithostatic chamber pressure (i.e. the chamber overpressure was equal to zero) to investigate the features of the conduit flow, such as the distributions of the overpressure, pressure, and gas volume fraction inside the conduit (Fig. 6b–d). The chamber pressure-magma flux relationship depends on permeability coefficient for gas escape (k_0), which leads to higher magma flux of the selected conduit flow for lower k_0 (Fig. 6a). The higher magma flux is caused by higher gas volume fraction or lower magma density in the conduit due to inefficient gas escape for lower k_0 (Fig. 6d): the gravitational load of magma is smaller for lower magma density, leading to lower resistance against the magma flow and higher magma flux.

The numerical results of the conduit flow show that an overpressure (with respect to the lithostatic pressure) is generated inside the conduit (Fig. 6b). This overpressure generation originates from magma vesiculation (Fig. 6d), which causes lower magma density, leading to a decrease in the magnitude of the pressure gradient in the region below the plug (Fig. 6c). The overpressure maximises in the region just beneath the plug (Fig. 6b). Figure 7 shows the depth at which the overpressure maximises as a function of k_0, with varying the conduit radius (r) and the aspect ratio of crystals (R_β). Here, k_0 was set in the range of 10^{-13}–10^{-10} m^2 to cover the reported permeabilities of the lava dome samples (Gonnermann and Manga 2007). The range of R_β was constrained from petrological data of the ash samples from Vulcanian eruptions at Sakurajima: the average aspect ratio of the plagioclase microlite ranges from 4 to 14 (Miwa et al. 2009). Since there is no direct information about the conduit radius, the range of r was widely set to 10–50 m. The results for $R_\beta = 4$ in the case of $r = 40$ and 50 m are not shown, because the magma flux was determined to be unrealistically high ($> 10^6$ kg s^{-1}). Under the above ranges of k_0, r, and R_β, the depth at which the overpressure maximises is approximately in the range of 0.4 to 1.0 km from the ground surface (i.e. crater floor) (Fig. 7). This depth is located just beneath the hypocentres of the explosion earthquakes occurring at the three craters.

Discussion

Recent analyses using data from multiple strain and tilt meters deployed at Sakurajima Volcano by Kyoto University indicate a pressure source depth of 0.5 km b.s.l. for about 3 min just after the 17 November 2017 eruption at Minamidake craters, followed by an inflation source at a depth of 0.5 km and long-term deflation at a depth of 3.3 km (Hotta and Iguchi 2021). The pressure sources for the eruptions in 2009 at Showa crater are located at depths between 0.5 and 1.5 km, as revealed by analyses of radial and tangential strains recorded at Arimura station, 2.2 km SSE of the crater (Iguchi et al. 2013). These values were estimated from the analytical solution of a spherical source for a semi-infinite homogeneous half space, although Hotta and Iguchi (2021) corrected the station elevation and source depths. To examine the effects of volcano topography, we numerically calculated the tilt, and radial and tangential strains generated by a pressure source beneath the summit, while approximating the volcano as a cone with a height of 1000 m and a radius of 5000 m at the base (Appendix 2). Results showed that the depth of the analytical solution can be directly converted to the depth from the summit crater for the analyses of strain data at a distance of more than 2 km caused by a spherical source (Mogi 1958) or a closed pipe (Bonaccorso and Davis 1999) (Figs. S7 and S8). Hence, the aforementioned

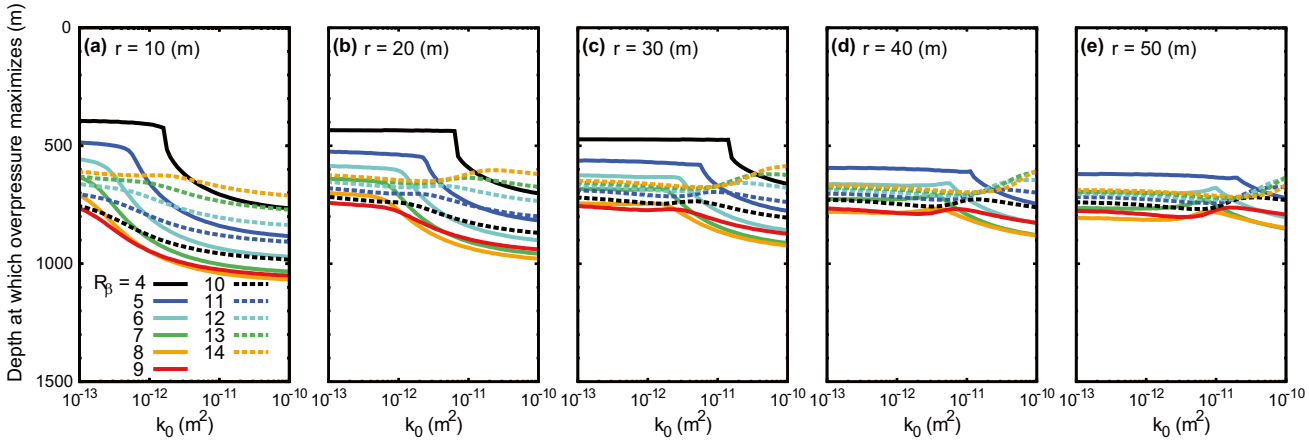

Fig. 7 Depth at which the overpressure in the conduit maximises as a function k_0 with varying R_β (=4–14) and r (=10 (**a**), 20 (**b**), 30 (**c**), 40 (**d**), and 50 (**e**) m), obtained from the one-dimensional steady conduit flow model

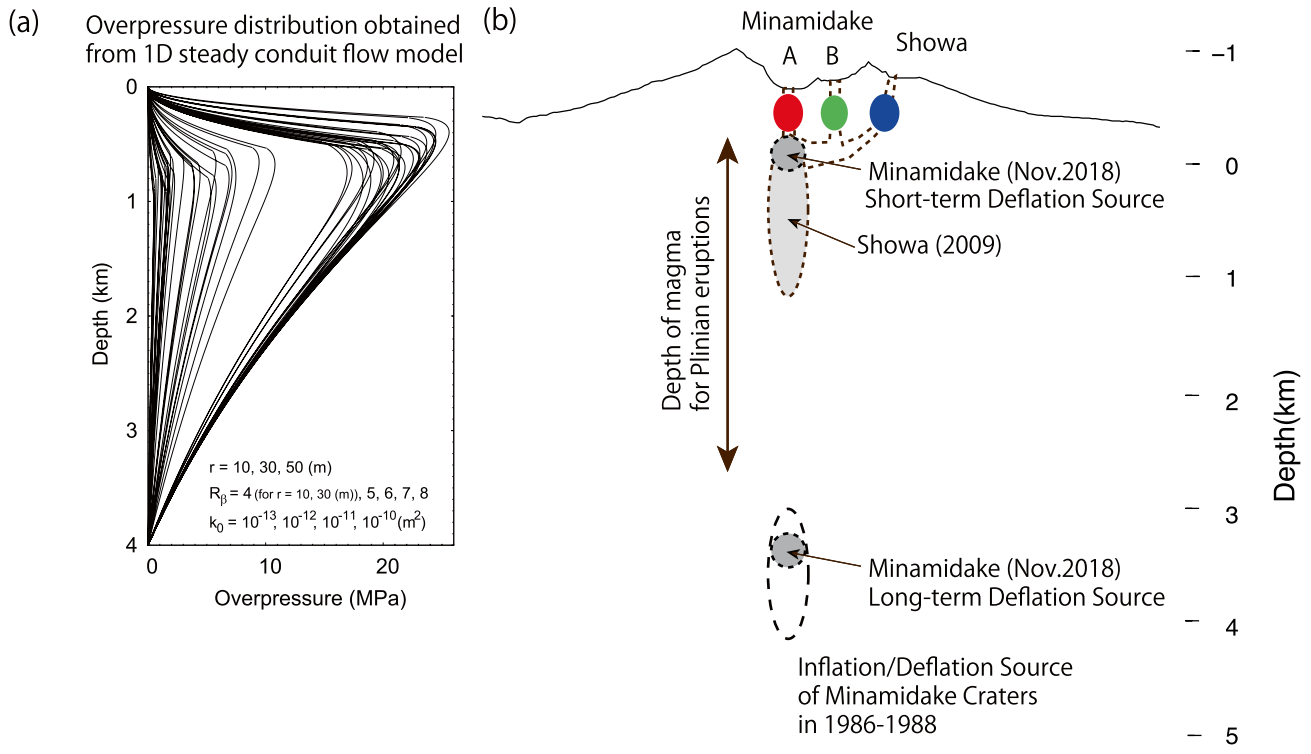

Fig. 8 **a** Overpressure distribution obtained from the one-dimensional steady conduit flow model, with varying r (10, 30, and 50 m), R_β (4, 5, 6, and 7), and k_0 (10^{-13}, 10^{-12}, 10^{-11}, and 10^{-10} m^2). **b** Schematic illustration of the magma supply system at Sakurajima Volcano. We note that the depth is taken from sea level but is adjusted vertically to the depth of the one-dimensional steady flow model. Red, green, and blue filled circles represent the eruption triggering points inferred from the hypocentre determination. Grey areas represent the pressure sources detected from geodetic measurements

source depths estimated in previous studies were converted to depths from the summit crater.

Figure 8 shows a schematic view of the magma and conduit system of the Vulcanian eruptions at Sakurajima Volcano. The hypocentres of the explosion earthquakes were located at a depth of a few hundred meters below each crater. Since the seismic moment of the P-wave of the explosion earthquake is estimated to be about 10^{10}–10^{11} N•m, which corresponds to an earthquake magnitude of 0.6–1.3, the seismic source region beneath each crater is explained by a sphere with a radius of 10–47 m and a pressure change of 0.1–1 MPa (Appendix 3). The radius is almost equal to the vent radius estimated from the video records and infrasound data (Muramatsu et al. 2018). The seismic source regions may be related to density changes that have recently been captured using muography (Oláh et al. 2019, 2023). Video observation detected temporal changes of the volcanic glow intensity approximately 1 s before an explosion, which is inferred to be related to the opening of tensile cracks on the crater floor before eruption (Muramatsu et al. 2023). Such a process appearing just before an explosion may be related to the lead times from the origin time of explosion earthquake to eruption. The overpressure region that is predicted from the one-dimensional conduit flow model, in which the depth at which the overpressure maximises is located in the range of 0.4 to 1.0 km from the crater floor (Fig. 7), is well matched with the inflation and deflation sources detected for about 3 min after the explosion by geodetic measurements, and is located just beneath the hypocentres of the explosion earthquakes occurring at the three craters. This suggests that the overpressure generated by the conduit flow triggers the explosion earthquakes. Based on these results, we infer the following mechanism of Vulcanian eruption: (1) Conduit flow generates overpressure inside the conduit due to magma vesiculation; (2) when the pressure reaches a critical level, a shallow region beneath the crater inflates to excite a P-wave; (3) the crater floor starts to deform due to the P-wave pressure and ruptures, resulting in eruption; (4) the volcanic materials are rapidly ejected to generate an explosion earthquake and infrasound, and rarefaction waves deflate the conduit and/or magma chamber beneath the Minamidake craters. Long-term deflation at a depth of 3.3 km (Hotta and Iguchi, 2021) may occur in case of a large eruption.

Some of the eruptions of Sakurajima Volcano were characterised by large magnitudes, for example the Plinian eruptions that occurred in 1471, 1779, and 1914 (Iguchi et al. 2020). Araya et al. (2019) inferred that the volcanic

materials erupted during these Plinian eruptions were stored at depths of 0.9–3.2 km beneath the crater based on the concentrations of volatiles in phenocryst-hosted melt inclusions and plagioclase rim equilibration. The storage regions were located below the inflation and deflation sources for Vulcanian eruptions, which suggests a different behaviour of the geodetic signals before and during eruptions (Fig. 8).

It should be noted that the hypocentres of explosion earthquakes in 1975–1976 (Nishi 1976) and in 1980–1986 (Ishihara 1990) as well as volcanic earthquakes called B-types associated with Strombolian eruptions in 1987–1988 (Iguchi 1994) were located at a depth of 0–2 km b.s.l. (ca. 1–3 km beneath the craters). These previous studies assumed a homogeneous structure with a P-wave velocity of 2.5 km/s, and determined their hypocentres using arrival times of 6–8 seismic stations deployed around the volcano. The newly determined hypocentres in this study are quite shallow (0.2–0.8 km beneath the craters) compared to those in previous studies. Because the hypocentres of the explosion earthquakes used in this study are located at 0–2 km b.s.l. when a homogeneous structure with a P-wave velocity of 2.5 km is assumed (Fig. S9), the seismic velocity model revealed from a seismic exploration is necessary to correctly determine the depths of the hypocentres and understand the eruption mechanism. The pressure source determined from analyses of tilt and strain meters at Harutayama station, which is 2.7 km west of Minamidake craters (Ishihara 1990), was estimated to be 2–6 km b.s.l. for the Vulcanian eruptions at Minamidake craters. Tateo and Iguchi (2009) estimated the inflation and deflation sources to be 3–4 km b.s.l for the Vulcanian eruptions and Strombolian eruptions accompanying BL-type earthquakes in 1986–1988. These pressure sources are much deeper than those determined for the 2012–2020 eruptions. This difference may be due to the difference of magnitude of eruption (the eruptions in 1980s are larger) and/or geodetic stations used in the analyses. Further observations and detailed comparison of the geodetic data can be used to compare them with the seismic results and numerical simulations to elucidate the magma system and conduit flow.

Conclusion

We have analysed seismic, infrasound, and tilt data associated with Vulcanian eruptions occurring at three active craters of Sakurajima Volcano. Precise hypocentre determination using a realistic seismic velocity structure deduced from artificial seismic experiments enabled us to locate the eruption triggering point at a shallow depth of approximately 0.5 km beneath each of the three craters. Infrasound data analysis indicates that swelling of the crater floor starts approximately 0.2 s after the origin time of explosion earthquake, and that the crater floor experiences an eruptive burst about 0.3 to 0.5 s later. No significant difference was observed between the explosions at the three craters, which suggests that the rupture processes and physical properties of their crater floors are similar. During an eruption, tilt vectors at a nearby station indicated a downward trend directed toward one of the three active craters. Whole rock analysis indicates that erupted material from the three craters is geochemically identical. We conclude that Vulcanian eruptions of all the three craters originate from a common shallow magma storage and conduit system. A one-dimensional steady conduit flow model predicts an overpressure at depths of approximately 0.4 to 1.0 km beneath the crater floor. The overpressure location is well matched with the inflation and deflation sources detected for about 3 min after the explosion by geodetic measurements in previous studies (Hotta and Iguchi, 2021). The overpressure region is also located just beneath the hypocentres of the explosion earthquakes occurring at the three craters. These results clarify the shallow magma conduit system consisting of triggering points separately locating beneath the three active craters and a common deflation source during eruption at Sakurajima Volcano. Since many volcanoes sometimes change their active craters and erupt with the same or different styles and magnitudes, our findings are useful for elucidating the eruption mechanisms of Sakurajima Volcano and other volcanoes around the world.

Appendix 1. One-dimensional steady conduit flow model

In this appendix, we show detailed formulations of the numerical simulation of one-dimensional steady conduit flow model. For the viscous flow region based on Kozono and Koyaguchi (2012), the mass conservation equations for the gas and the liquid-crystals phases are expressed as

$$\pi r^2 \phi \rho_g w_g = nQ, \tag{1}$$

and

$$\pi r^2 (1-\phi)\left[(1-\beta)\rho_l + \beta\rho_c\right] w_l = (1-n)Q, \tag{2}$$

respectively, and the momentum conservation equations for the gas and the liquid-crystals phases are expressed as

$$0 = -\phi\frac{dp}{dz} - \phi\rho_g g - F_{lg}, \tag{3}$$

and

$$0 = -(1-\phi)\frac{dp}{dz} - (1-\phi)\left[(1-\beta)\rho_l + \beta\rho_c\right] g + F_{lg} - F_{lw}, \tag{4}$$

respectively, in which the inertia terms are assumed to be negligible. Here, r is the conduit radius, ϕ is the gas volume

fraction (porosity), ρ is the density, w is the velocity, β is the crystal volume fraction (crystallinity), n is the mass-flow-rate fraction of gas, Q is the magma flux in kg s^{-1}, p is the pressure, g is the acceleration due to gravity, and the subscripts g, l, and c for ρ and w denote the gas, liquid, and crystal phases, respectively. The gas density (ρ_g) is expressed as

$$\rho_g = \frac{p}{RT}, \tag{5}$$

where R is the gas constant, and T is the temperature. The liquid and crystal densities (ρ_l and ρ_c) are assumed to be constant (= 2500 kg m^{-3}). The mass-flow-rate fraction of the gas is expressed as

$$n = \frac{n_0 - n_l c}{1 - n_l c}, \tag{6}$$

where n_l is the mass fraction of the liquid with respect to the liquid-crystals mixture expressed by

$$n_l = \frac{(1-\beta)\rho_l}{(1-\beta)\rho_l + \beta\rho_c}, \tag{7}$$

and c is the dissolved H_2O.

The momentum conservation equations include two external forces: the interaction force between the gas and the liquid-crystals mixture (F_{lg}), and the friction force between the liquid-crystals mixture and the conduit wall (F_{lw}). The forms of these forces are formulated as

$$F_{lg} = \frac{\eta_g}{k}\phi^2\left(w_g - w_l\right), \tag{8}$$

and

$$F_{lw} = \frac{8\eta}{r^2}w_l, \tag{9}$$

where η_g is the gas viscosity (set to 10^{-5} Pa s), k is the gas permeability in the magma, and η is the magma viscosity. The form of k is expressed following Costa (2006) as

$$k = k_0\frac{\phi^3}{1-\phi}, \tag{10}$$

where k_0 is the constant representing the permeability scale. The magma viscosity is controlled by various factors such as composition, temperature, and crystallinity, and it is formulated as

$$\eta = \eta_l \eta_r'\left(\beta, R_\beta, \dot{\varepsilon}\right), \tag{11}$$

where η_l is the liquid viscosity, and η_r' represents the non-dimensional relative viscosity describing the viscosity dependence on β, the aspect ratio of the crystals R_β, and the strain rate $\dot{\varepsilon}$ formulated by Frontoni et al. (2022), where $\dot{\varepsilon}$ is calculated from w_l/r in this study. Although the viscosity also depends on the porosity in a complex manner (Llewellin et al. 2002), we do not consider this effect because the porosity is not so high in the conduit during no-eruption phase.

The fitting functions for the equilibrium crystallinity of microlites (β_{eq}), the dissolved H_2O (c), and the liquid viscosity (η_l), which were constrained from the rhyolite-MELTS program, are formulated as

$$\beta_{eq} = C_{\beta_0}\exp\left(C_{\beta_1}p\right), \tag{12}$$

$$c = sp^m, \tag{13}$$

and

$$\log_{10}\eta_l = C_{\eta_0} + C_{\eta_1}c + C_{\eta_2}c^2 + C_{\eta_3}c^3, \tag{14}$$

where the constants are set as follows: $C_{\beta 0} = 0.425$; $C_{\beta 1} = -4.63\times10^{-8}$ Pa^{-1}; $s = 7.27\times10^{-7}$ $Pa^{-0.586}$; and $m = 0.586$; $C_{\eta 0} = 6.98$; $C_{\eta 1} = -2.56\times10^{2}$; $C_{\eta 2} = 6.85\times10^{3}$; and $C_{\eta 3} = -7.32\times10^{4}$. The total crystallinity β is calculated as $\beta_{ph} + (1-\beta_{ph})\beta_{eq}$, where β_{ph} is the crystallinity at the magma chamber (i.e. phenocryst volume fraction). The functions of Eqs. (12), (13), and (14) are shown in Fig. S5.

For the solid plug region based on Anderson and Segall (2011), the force balance at the solid plug is expressed as:

$$0 = \left(p_p - p_a\right)r - \rho_p r H_p g - 2H_p\tau_p, \tag{15}$$

where p_p is the pressure at the plug base, p_a is the atmospheric pressure, ρ_p is the plug density (set to 2500 kg m^{-3}), H_p is the plug height, and τ_p is the velocity-dependent shear stress on the margin of the plug. Here, τ_p is expressed as

$$\tau_p = a\bar{\sigma}\,\mathrm{arcsinh}\left(\frac{w_p}{2w_r}\exp\frac{f_0}{a}\right), \tag{16}$$

where w_p is the sliding velocity, f_0 is the coefficient of friction (set to 0.4) at the reference sliding velocity w_r (set to 0.001 m s^{-1}), a is the direct effect (set to 0.08), and $\bar{\sigma}$ is the mean effective normal stress (depth average of normal stress minus pore fluid pressure) on the sliding surfaces:

$$\bar{\sigma} = \sigma_c\rho_l g H_p/2, \tag{17}$$

where σ_c is a coefficient relating lithostatic pressure to normal stress on the plug (set to 0.3).

The critical condition for the transition from the viscous flow to the solid plug is expressed as

$$\left.\frac{8\eta w_l}{r^2}\right|_{z=-H_p} = \left.\frac{2\tau_p}{r}\right|_{z=-H_p}. \tag{18}$$

At the boundary of the viscous flow and the solid plug, the following relationship for the mass conservation should be satisfied:

$$\rho_p w_p = \left[\phi\rho_g w_g + (1-\phi)\{(1-\beta)\rho_l + \beta\rho_c\}w_l\right]\Big|_{z=-H_p}. \quad (19)$$

The equations for the viscous flow are solved to satisfy the boundary conditions at the bottom (i.e. magma chamber) and the top (i.e. the plug base) ends of the flow with a length of $L_{total} - Hp$ where L_{total} is the conduit length. The boundary condition at the bottom is the pressure at the magma chamber, and the flow variables (p, w_g, w_l, ϕ, and β) at the top of the flow (i.e. the plug base) should satisfy Eqs. (18) and (19).

Appendix 2. Effect of volcano topography on ground deformation

We numerically investigated the effect of volcano topography on ground deformation caused by a pressure source beneath the summit, based on the finite element method (COMSOL Multiphysics® software). A homogeneous elastic medium was modelled by assuming axial symmetry, and the topography of Sakurajima Volcano was approximated by a cone with a height of 1000 m and a radius of 5000 m. The entire size of the medium, which was characterised by the depth and horizontal distance from the vent, was set to 300 km to eliminate any boundary effects on the calculation. The pressure source was assumed to be a sphere or closed pipe located just below the summit. The numerical results of the ground deformation (tilt, and radial and tangential strains) were compared with the analytical solutions for a semi-infinite elastic medium with a flat surface (Mogi 1958; Bonaccorso and Davis 1999) to assess the effect of the volcano topography (Figs. S7 and S8). In the case of a spherical source, the distance and displacement were normalised by the source depth and the analytical solution of the vertical displacement at the surface above the source, respectively (Fig. S7). In the case of the closed pipe, the distance was normalised by the depth of the top of the pipe (d_1), and the displacement was normalised by the analytical solution of the vertical displacement at the surface above the source in the $d_2 \to \infty$ limit, where d_2 is the depth of the bottom of the pipe (Fig. S8). We set d_1 and d_2 to 500 m and 1000–1500 m, respectively, to cover the observed range of the source depth. The pipe radius was varied in the range of 10–50 m.

Appendix 3. Estimation of the source parameters of the P-waves of explosion earthquakes

From the velocity amplitudes of the P-waves and the pulse width of the P-waves (approximately 0.2 s), the displacement of the P-waves was estimated to be approximately 10^{-7}–10^{-6} m at Amidagawa station. Assuming a hypocentral distance of 2.7 km, P-wave velocity of 2.5 km/s, and density of the structure of 2700 kg/m^3, we estimated the seismic moment (M_o) to be about 10^{10}–10^{11} N•m, which is equivalent to a seismic magnitude of 0.6–1.3. Assuming a spherical pressure source for the P-wave generation (Tameguri et al. 2002) and a pressure increase ΔP of 0.1–1.0 MPa, which was substituted from the estimation of the main phase of explosion earthquakes (Nishimura 1998), a radius (a) of 10–47 m was estimated from the relation $M_o = 3\pi a^3 \Delta P$ (Kanamori et al. 1984). If the fault was a source, the fault length and slip amount were estimated to be 3–8 m and < 1 mm, respectively.

Supplementary Information The online version contains supplementary material available at https://doi.org/10.1007/s00445-024-01722-y.

Acknowledgements We used seismic, infrasound, and tilt data from the Japan Meteorological Agency, and the explosion and eruption list at the Sakurajima Volcano of the Kagoshima Meteorological Office. We thank Prof. T. Kobayashi (Kagoshima University) and the Japan Meteorological Agency for providing some of the volcanic lapilli samples. Careful comments from anonymous reviewers improved the manuscript.

Funding This study was partly supported by the Ministry of Education, Culture, Sports, Science, and Technology (MEXT) of Japan under The Second Earthquake and Volcano Hazards Observation and Research Program (Earthquake and Volcano Hazard Reduction Research), a grant from the Integrated Program for Next Generation Volcano Research and Human Resource Development, and JSPS KAKENHI Grant Number 22H01318.

Data availability Seismic, infrasound, and tilt data are available from the website of the National Research Institute for Earth Science and Disaster Resilience in Japan (https://www.hinet.bosai.go.jp/?LANG=en).

Code availability All codes are available upon request.

Declarations

Competing interests The authors declare no competing interests.

Open Access This article is licensed under a Creative Commons Attribution 4.0 International License, which permits use, sharing, adaptation, distribution and reproduction in any medium or format, as long as you give appropriate credit to the original author(s) and the source, provide a link to the Creative Commons licence, and indicate if changes were made. The images or other third party material in this article are included in the article's Creative Commons licence, unless indicated otherwise in a credit line to the material. If material is not included in the article's Creative Commons licence and your intended use is not permitted by statutory regulation or exceeds the permitted use, you will need to obtain permission directly from the copyright holder. To view a copy of this licence, visit http://creativecommons.org/licenses/by/4.0/.

References

Anderson K, Segall P (2011) Physics-based models of ground deformation and extrusion rate at effusively erupting volcanoes. J Geophys Res 116:B07204. https://doi.org/10.1029/2010JB007939

Araya N, Nakamura M, Yasuda A et al (2019) Shallow magma precharge during repeated Plinian eruptions at Sakurajima Volcano. Sci Rep 9:1979. https://doi.org/10.1038/s41598-019-38494-x

Bonaccorso A, Davis PM (1999) Models of ground deformation from vertical volcanic conduits with application to eruptions of Mount St Helens and Mount Etna. J Geophys Res 104:10531–10542. https://doi.org/10.1029/1999JB900054

Chouet B, Dawson P, Arciniega-Ceballos A (2005) Source mechanism of Vulcanian degassing at Popocatépetl volcano, Mexico, determined from waveform inversions of very long period signals. J Geophys Res 110:B07301. https://doi.org/10.1029/2004JB003524

Clarke AB, Ongaro TE, Belousov A (2015) Vulcanian eruptions. In: Sigurdsson H (ed) The encyclopedia of volcanoes, 2nd edn. Elsevier, London, pp 505–518

Costa A (2006) Permeability-porosity relationship: a reexamination of the Kozeny-Carman equation based on a fractal pore-space geometry assumption. Geophys Res Lett 33:L02318

de Kool M, Rawlinson N, Sambridge M (2006) A practical grid-based method for tracking multiple refraction and reflection phases in 3D heterogeneous media. Geophys J Int 167:253–270. https://doi.org/10.1111/j.1365-246X.2006.03078.x

Dzurisin D (2007) Volcano deformation: geodetic monitoring techniques. Springer, Chichester, UK

Frontoni A, Costa A, Vona A, Romano C (2022) A comprehensive database of crystal-bearing magmas for the calibration of a rheological model. Sci Data 9:247. https://doi.org/10.1038/s41597-022-01363-w

Giordano D, Russell JK, Dingwell DB (2008) Viscosity of magmatic liquids: a model. Earth Planet Sci Lett 271:123–134. https://doi.org/10.1016/j.epsl.2008.03.038

Gonnermann HM, Manga M (2007) The fluid mechanics inside a volcano. Annu Rev Fluid Mech 39:321–356. https://doi.org/10.1146/annurev.fluid.39.050905.110207

Gualda GAR, Ghiorso MS, Lemons RV, Carley TL (2012) Rhyolite-MELTS: a modified calibration of MELTS optimized for silica-rich, fluid-bearing magmatic systems. J Petrol 53:875–890. https://doi.org/10.1093/petrology/egr080

Hotta K, Iguchi M (2021) Tilt and strain change during the explosion at Minami-dake, Sakurajima, on November 13, 2017. Earth Planets Space 73:70. https://doi.org/10.1186/s40623-021-01392-6

Hreinsdóttir S, Sigmundsson F, Roberts M et al (2014) Volcanic plume height correlated with magma-pressure change at Grímsvötn Volcano, Iceland. Nature Geosci 7:214–218. https://doi.org/10.1038/ngeo2044

Ichihara M, Kameda M (2004) Propagation of acoustic waves in a visco-elastic two-phase system: influences of the liquid viscosity and the internal diffusion. J Volcanol Geotherm Res 137:73–91. https://doi.org/10.1016/j.jvolgeores.2004.05.002

Iguchi M (1994) A vertical expansion source model for the mechanism of earthquakes originated in the magma conduit of an andesitic volcano: Sakurajima, Japan. Bull Volcanol Soc Jpn 39:49–67

Iguchi M (2016) Method for real-time evaluation of discharge rate of volcanic ash – case study on intermittent eruptions at the Sakurajima Volcano, Japan. J Disaster Res 11:4–14. https://doi.org/10.20965/jdr.2016.p0004

Iguchi M, Tameguri T, Ohta Y, Ueki S, Nakao S (2013) Characteristics of volcanic activity at Sakurajima Volcano's Showa crater during the period 2006 to 2011. Bull Volcanol Soc Jpn 58:115–135. https://doi.org/10.18940/kazan.58.1_115

Iguchi M, Nakamichi H, Tanaka HL, Ohta Y, Shimizu A, Miki D (2019) Integrated monitoring of volcanic ash and forecasting at Sakurajima Volcano, Japan. J Disaster Res 14:798–809. https://doi.org/10.20965/jdr.2019.p0798

Iguchi M, Nakamichi H, Tameguri T (2020) Integrated study on forecasting volcanic hazards of Sakurajima Volcano, Japan. J Disaster Res 15:174–186. https://doi.org/10.20965/jdr.2020.p0174

Inza LA, Métaxian JP, Mars JI, Bean CJ, O'Brien GS, Macedo O, Zandomeneghi D (2014) Analysis of dynamics of Vulcanian activity of Ubinas volcano, using multicomponent seismic antennas. J Volcanol Geotherm Res 270:35–52. https://doi.org/10.1016/j.jvolgeores.2013.11.008

Ishihara K (1985) Dynamical analysis of volcanic explosion. J Geodynamics 3:327–349

Ishihara K (1990) Pressure sources and induced ground deformation associated with explosive eruptions at an andesitic volcano: Sakurajima Volcano, Japan. In: Ryan MP (ed) Magma transport and storage. Wiley, pp 335–356

Ishii K, Yokoo A (2021) Combined approach to estimate the depth of the magma surface in a shallow conduit at Aso volcano. Japan Earth Planets Space 73:187. https://doi.org/10.1186/s40623-021-01523-z

Kamo K, Ishihara K (1986) Precursor of summit eruption observed by water-tube tiltmeters and extensometers. Ann Disas Prev Res Inst Kyoto Univ. 29:1–12 (in Japanese with English abstract)

Kanamori K, Given JW (1983) Lamb pulse observed in nature. Geophys Res Lett 10:373–376. https://doi.org/10.1029/GL010i005p00373

Kanamori H, Given JW, Lay T (1984) Analysis of seismic body waves excited by the Mount St Helens eruption of May 18, 1980. J Geophys Res 89:1856–1866. https://doi.org/10.1029/JB089iB03p01856

Kieffer S (1984) Seismicity of Old Faithful Geyser: an isolated source of geothermal noise and possible analogue of volcanic seismicity. J Volcanol Geotherm Res 22:59–95. https://doi.org/10.1016/0377-0273(84)90035-0

Kim K, Lees JM, Ruiz M (2012) Acoustic multipole source model for volcanic explosions and inversion for source parameters. Geophys J Int 191:1192–1204. https://doi.org/10.1111/j.1365-246X.2012.05696.x

Kim K, Lees JM, Ruiz MC (2014) Source mechanism of Vulcanian eruption at Tungurahua Volcano, Ecuador, derived from seismic moment tensor inversions. J Geophys Res Solid Earth 119:1145–1164. https://doi.org/10.1002/2013JB010590

Kobayashi T, Miki D, Sasaki H, Iguchi M, Yamamoto T, Uto K (2013) Geological map of Sakurajima Volcano, 2nd edn. Geological Survey of Japan, AIST, Tsukuba (in Japanese with English abstract)

Kozono T, Koyaguchi T (2012) Effects of gas escape and crystallization on the complexity of conduit flow dynamics during lava dome eruptions. J Geophys Res 117:B08204. https://doi.org/10.1029/2012JB009343

Kozono T, Ueda H, Shimbori T et al (2014) Correlation between magma chamber deflation and eruption cloud height during the 2011 Shinmoe-dake eruptions. Earth Planet and Space 66:139. https://doi.org/10.1186/s40623-014-0139-1

Llewellin EW, Mader HM, Wilson SDR (2002) The rheology of a bubbly liquid. Proc R Soc Lond A 458:987–1016. https://doi.org/10.1098/rspa.2001.0924

Lyon JJ, Waite GP (2011) Dynamics of explosive volcanism at Fuego volcano imaged with very long period seismicity. J Geophys Res 116:B09303. https://doi.org/10.1029/2011JB008521

Maki M, Suzuki I, Iguchi M, Shakti PC (2019) Quantitative volcanic ash fall estimation by weather radar: Z-RA relationship for the Sakurajima eruption of August 18, 2013. Bull Volcanol Soc Jpn 64:219–241. https://doi.org/10.18940/kazan.64.4_219

Marchetti E, Ichihara M, Ripepe M (2004) Propagation of acoustic waves in a viscoelastic two-phase system: influence of gas bubble concentration. J Volcanol Geotherm Res 137:93–108. https://doi.org/10.1016/j.jvolgeores.2004.05.002

Matsumoto A, Nakagawa M, Amma-Miyasaka M, Iguchi M (2013) Temporal variations of the petrological features of the juvenile materials during 2006 to 2010 from Showa Crater, Sakurajima Volcano, Kyushu, Japan. Bull Volcanol Soc Jpn 58:191–212. https://doi.org/10.18940/kazan.58.1_191

Matsumoto A, Nakagawa M, Iguchi M (2016) The 24th July, 2012 eruption from the Minamidake summit crater at Sakurajima Volcano, inferred from groundmass textures of juvenile materials in the volcanic ash, especially features of microlite. Bull Volcanol Soc Jpn 61: 545–558. 10.18940/kazan.61.3_545Medici EF, Allen JS, Waite GP (2014) Modeling shock waves generated by explosive volcanic eruptions. Geophys Res Lett 41:414–421. https://doi.org/10.1002/2013GL058340

Médici EF, Allen JS, Waite GP (2014) Modeling shock waves generated by explosive volcanic eruptions. Geophys Res Lett 41:414–421. https://doi.org/10.1002/2013GL058340

Miwa T, Toramaru A, Iguchi M (2009) Correlations of volcanic ash texture with explosion earthquakes from Vulcanian eruptions at Sakurajima Volcano, Japan. J Volcanol Geotherm Res 184:473–486. https://doi.org/10.1016/j.jvolgeores.2009.05.012

Miwa T, Geshi N, Shinohara H (2013) Temporal variation in volcanic ash texture during a Vulcanian eruption at the Sakurajima Volcano, Japan. J Volcanol Geotherm Res 260:80–89. https://doi.org/10.1016/j.jvolgeores.2013.05.010

Miyamachi H et al (2013) Shallow velocity structure beneath the Aira Caldera and Sakurajima Volcano as inferred from refraction analysis of the seismic experiment in 2008. Bull Volcanol Soc Jpn 58:227–237. https://doi.org/10.18940/kazan.58.1_227

Mogi K (1958) Relations between the eruptions of various volcanoes and the deformations of the ground surfaces around them. Bull Earthquake Res Inst Univ Tokyo 36:99–134

Morrissey M, Chouet BA (1997) Burst conditions of explosive volcanic eruptions recorded on microbarographs. Science 275:1290–1293. https://doi.org/10.1126/science.275.5304.1290

Muramatsu D, Aizawa K, Yokoo A, Iguchi M, Tameguri T (2018) Estimation of vent radii from video recordings and infrasound data analysis: implications for Vulcanian eruptions from Sakurajima Volcano, Japan. Geophys Res Lett 45:12–829

Muramatsu D, Aizawa K, Yokoo A, Tameguri T, Iguchi M (2023) Vulcanian eruption processes inferred from volcanic glow analysis at Sakurajima Volcano. Japan Bull Volcanol 85:41. https://doi.org/10.1007/s00445-023-01656-x

Nishi K (1976) On the explosion earthquake of Sakurajima Volcano. Annuals Disas Prev Res Inst Kyoto Univ B-1 19:69–73

Nishimura T (1998) Source mechanisms of volcanic explosion earthquakes: single force and implosive sources. J Volcanol Geotherm Res 86:97–106

Nishimura T, Hamaguchi H (1993) Scaling law of volcanic explosion earthquake. Geophys Res Lett 20:2479–2482

Nishimura T, Iguchi M (2011) Volcanic earthquakes and tremor in Japan. Kyoto University Press, Kyoto, Japan

Nishimura T, Iguchi M, Kawaguchi R, Surono HM, Rosadi U (2012) Inflations prior to Vulcanian eruptions and gas bursts detected by tilt observations at Semeru Volcano, Indonesia. Bull Volcanol 74:903–911. https://doi.org/10.1007/s00445-012-0579-z

Nishimura T, Iguchi M, Yakiwara H, Oikawa J, Kawaguchi R, Aoyama H, Nakamichi H, Ohta Y, Tameguri T (2013) Mechanism of small Vulcanian eruptions at Suwanosejima Volcano, Japan, as inferred from precursor inflations and tremor signals. Bull Volcanol 75:779. https://doi.org/10.1007/s00445-013-0779-1

Ohminato T, Takeo M, Kumagai H et al (2006) Vulcanian eruptions with dominant single force components observed during the Asama 2004 volcanic activity in Japan. Earth Planet Space 58:583–593. https://doi.org/10.1186/BF03351955

Oláh L, Tanaka HKM, Ohminato T, Hamar G, Varga D (2019) Plug formation imaged beneath the active craters of Sakurajima Volcano with muography. Geophys Res Lett 46:10417–10424. https://doi.org/10.1029/2019GL084784

Oláh L, Gallo G, Hamar G, Kamoshida O, Leone G, Llewellin EW, Presti DL, Nyitrai G, Ohminato T, Ohno S, Tanaka HKM, Dezső Varga D (2023) Muon imaging of volcanic conduit explains link between eruption frequency and ground deformation. Geophys Res Lett 50:e2022GL101170. https://doi.org/10.1029/2022GL101170

Putirka KD (2008) Thermometers and barometers for volcanic systems. Rev Mineral Geochem 69:61–120. https://doi.org/10.2138/rmg.2008.69.3

Ripepe M, Ciliberto S, Schiava MD (2001) Time constraints for modeling source dynamics of volcanic explosions at Stromboli. J Geophys Res 106:8713–8727

Schneider A, Rempel AW, Cashman KV (2012) Conduit degassing and thermal controls on eruption styles at Mount St Helens. Earth Planet Sci Lett 357–358:347–354. https://doi.org/10.1016/j.epsl.2012.09.045

Sugimura S, Nishimura T, Lacanna G, Legrand D, Valade S, Ripepe M (2021) Seismic source migration during Strombolian eruptions inferred by very-near-field broadband seismic network. J Geophys Res 126:e2021JB022623. https://doi.org/10.1029/2021JB022623

Tameguri T, Iguchi M, Ishihara K (2002) Mechanism of explosive eruptions from moment tensor analyses of explosion earthquakes at Sakurajima Volcano, Japan. Bull Volcanol Soc Jpn 47:197–215. https://doi.org/10.18940/kazan.47.4_197

Tateo Y, Iguchi M (2009) Ground deformation associated with BL-type earthquake swarms at Sakurajima Volcano. Bull Volcanol Soc Jpn 54:175–186

Watson LM, Iezzi AM, Toney L et al (2022) Volcano infrasound: progress and future directions. Bull Volcanol 84:44. https://doi.org/10.1007/s00445-022-01544-wZobinVM(2016)Introductiontovolcanicseismology,3rdedition.Elsevier

Yamada T, Aoyama H, Nishimura T, Yakiwara H, Nakamichi H, Oikaw J, Iguchi M, Hendrasto M, Suparman Y (2016) Initial phases of explosion earthquakes accompanying Vulcanian eruptions at Lokon-Empung volcano, Indonesia. J Volcanol Geotherm Res 327:310–321. https://doi.org/10.1016/j.jvolgeores.2016.08.011

Yokoo A, Tameguri T, Iguchi M (2009) Swelling of a lava plug associated with a Vulcanian eruption at Sakurajima Volcano, Japan, as revealed by infrasound record: case study of the eruption on January 2, 2007. Bull Volcanol 71:619–630. https://doi.org/10.1007/s00445-008-0247-5

Zobin VM (2016) Introduction to volcanic seismology, 3rd edn. Elsevier

Zobin VM, Reyes GA, Guevara E, Bretón M (2008) Seismological constraints on the position of the fragmentation surfaces in the volcano conduit. Earth Planet Sci Lett 275:337–341. https://doi.org/10.1016/j.epsl.2008.08.034